Analytical and magnetic characterization of the pyrite Carbothermic reduction in the presence of lime

O. K. Ilunga^{1*}, O. T. Johnson^{1,2}, F. P. L Kavishe^{1**}, K. K. Alaneme³

Abstract

Pyrite (FeS₂) is a major by-product of copper flotation, primarily used for sulphuric acid production, with its residual cinders often disposed of as waste, posing environmental challenges. This study investigates the carbothermic reduction of pyrite in the presence of lime, focusing on iron metallization, sulphur retention, reaction kinetics, and magnetic characterization to explore its potential as an alternative iron source. A systematic experimental approach was employed, assessing thermal decomposition, ion exchange, and carbothermic reduction stages at different temperatures (1273K, 1373K, and 1473K), treatment times (5–25 min), and C/CaO ratios. The results indicate that thermal decomposition exhibited the highest mass loss due to sulphur volatilization, while ion exchange effectively captured sulphur as CaS, reducing SO₂ emissions. At the carbothermic reduction stage, iron metallization improved with increasing C/CaO ratio, but liquid phase formation hindered reaction kinetics by restricting gas diffusion. Reaction kinetics analysis showed that thermal decomposition followed zero-order kinetics at 1273K and second-order kinetics at 1373K and 1473K, confirming temperaturedependent reaction mechanisms. Magnetic susceptibility tests revealed that iron-bearing phases transformed, with magnetic phases present at lower temperatures and non-magnetic metallic iron dominating at higher temperatures. These findings demonstrate the potential for pyritebased iron production, offering a sustainable alternative to high-grade iron ore while minimizing environmental pollution. Future research should focus on scaling up the process, optimizing energy efficiency, and exploring by-product utilization for industrial applications.

Keywords: Pyrite reduction; Iron metallization; Carbothermic reductions; Reaction kinetics; Magnetic characterization.

Received: January 2024

Received in revised form: June 2025

Accepted: November 2025 Published: November 2025

1 INTRODUCTION

Pyrite (FeS₂) is a common sulphide mineral, often occurring alongside copper, zinc, lead, and arsenic-bearing minerals in sulphide deposits. While copper remains the primary economic target, pyrite is mainly utilized for sulphuric acid (H₂SO₄) production, accounting for approximately 67% of its global utilization (Giunti, 2004; Zheng, 2011). However, the pyrite cinders remaining after sulphur extraction present challenges due to their complex mineralogy, lower residual iron content (~47%), and potential environmental hazards arising from heavy metal impurities (Hongming, 2014; Qiang et al., 2019; Tugrul et al., 2006, 2007). These factors limit their direct application in the iron and steel industries.

¹Department of Mechanical & Metallurgical Engineering, School of Engineering & Built Environment, University of Namibia, Ongwediva, Namibia, Tel: +264652324000, Fax: +26488528466 P. O. Box 3624, Namibia, oilunga@unam.na

² Department of Chemical and Materials Engineering, University of South Africa, Pretoria, South Africa ³Federal University of Technology, Department of Metallurgical and materials Engineering Akure, Nigeria, kkalaneme@futa.edu.ng

The disposal of pyrite cinders poses significant environmental risks, including soil contamination and acid drainage. Despite efforts to utilize pyrite cinders in applications such as brick pigmentation, cement additives, and paint production (Abdrakhimov et al., 2006; Chun et al., 2011), their large-scale disposal remains a challenge. The increasing demand for sustainable metallurgical processes has driven interest in alternative methods for iron recovery from pyrite, particularly through direct reduction processes, which require lower energy inputs compared to conventional blast furnace operations (Ahindra, 2008; Alpi et al., 2009; Liu et al., 2011).

Previous studies have demonstrated the potential of pyrite as an iron source through roasting and carbothermic reduction. For instance, Kama et al. (2021) achieved an iron upgrade from 29.59% to 52.72% in pyrite concentrate subjected to roasting at 1073K and subsequent carbothermic reduction at 1373K. The main reduction reactions, as described by Turkdogan (1996), involved direct and indirect reduction of iron oxides with carbon monoxide and carbon, respectively as shown in Eq. 1 & 2. Such oxides reduction kinetics is based on the weight-loss method under isothermal conditions and a steady flow of a reducing gas of a constant composition, or analytical based on iron and sulphur concentrations (Sun, 2009).

$$Fe_2O_3 + C = Fe + CO \quad \Delta G_T = 699.7 - 336.5 \text{T kJ/mol}$$
 (1)
 $2FeO + 2C = 2Fe + CO_2 \quad \Delta G_T = 132.1 - 129.1 \text{T kJ. mol}^{-1}$ (2)

Similarly, Hara (2013, 2014) investigated the metallization of iron from complex sulphide ores using ion exchange and carbothermic reduction, highlighting the role of chalcocite (Cu₂S) as a catalytic agent in promoting the formation of intermediate calcium ferrite phases. However, these studies primarily focused on complex sulphides containing significant non-ferrous metals, leaving a gap in knowledge regarding the direct reduction of high-purity pyrite without the influence of copper or cobalt. Industrial viability requires further improvements, including enhanced sulphur removal, increased iron grade, and the mitigation of process complexity caused by mineralogical variability (Zhu et al., 2006; Zheng et al., 2012; Rath, 2017; Zorya et al., 2015).

To address these challenges, this study investigates the carbothermic reduction of pyrite concentrate in the presence of lime, a process that enables simultaneous iron metallization and sulphur capture. Lime acts as a desulphurization agent, promoting the formation of calcium sulphide (CaS) instead of gaseous SO₂ emissions, thus aligning with environmentally sustainable metallurgical practices (Denis, 2015). Additionally, understanding the reaction kinetics and phase transformations is essential for optimizing the process. Thermal decomposition, ion exchange, and carbothermic reduction stages are evaluated at different temperatures (1273K, 1373K, and 1473K) and C/CaO ratios, with an emphasis on reaction mechanisms, kinetics, and the impact of lime on sulphur retention.

Furthermore, magnetic characterization of the reduced products provides insights into phase transformations, which are critical for downstream processing and iron recovery. This study contributes to the broader goal of sustainable mining and metallurgical processing by offering a viable pathway to repurpose pyrite cinders for iron extraction while reducing environmental pollution. The findings hold potential for applications in the steel industry, particularly in direct reduced iron (DRI) production, as a cost-effective and energy-efficient alternative to conventional iron ore-based processes.

1.1 Thermal decomposition

A study on iron disulphide behaviour at high temperature, found that pyrite thermal decomposition starts at 873K, but other investigation on the melting point of the pyrite suggested instead that this material melts at 876K, which is much closer to the decomposition temperature (Kipp, 2018; Knovel, 2023). In support to the decomposition thesis, on roasting pyrite chemistry publication Mular et al. (2002) argues that even in oxidizing conditions, when SO₂ concentration in the gas exceeds 5%, pyrite decomposes to pyrrhotite (FeS_x), through reaction as presented in Eq. (3) (Pelovski, 1999),

$$nFeS_2 \rightarrow Fe_nS_{n+1} + (n-1)S \tag{3}$$

While agreeing with Mular et al. (2002) and Lambert (1998), other accepted equilibra suggest that thermal decomposition takes place in temperature range 523K - 1016 K and gives pyrrhotite (FeS_x) where x takes different values between 1 and 1.23 following Eq. (4). Lambert (1998) suggests that x takes values of 1.090, 1.105, 1,140 and 1.152 (Lambert et al., 1998):

$$x = 4.3739 \times 10^{-12} T^4 - 1.2034 \times 10^{-8} T^3 + 1.2365 \times 10^{-5} T^2 - 5.4779 \times 10^{-3} T + 1.99$$
 (4)

Pyrite thermal decomposition in air – gas mixture was investigated and reactions were described as two stages ruptures of chained weaker bonds similar to Van Der Waals between iron and sulphur, the first in the temperature range 683 - 961K (Pelovski, 1999), with subsequent formation of a non stokiometric pyrrhotite iron sulphide (Fe_{1-x}S), trilolite forms specifically in the range 683 - 789 K according to reaction in Eq. (5), their activation energy is in the range of 120 - 275 kJ/mol,

$$FeS_2 = FeS + S \tag{5}$$

Similar behavior was confirmed by (Hara, 2014), where pyrite decomposes into troilite which melts at 1463K, he presented mechanism as shows reaction in Eq. (6):

$$4.5 \text{FeS}_2 = 4.5 \text{FeS} + 2.25 \text{S}_2$$
 $\Delta G_T = 289.23 - 3.34 \text{T kJ/mol}$ (6)

In addition, (Changshun et al., 2022) reported extensive investigation on pyrite thermal decomposition, their findings revealed that thermal decomposition of pyrite is controlled by a chemical reaction and is a surface first-order reaction and proceeds in the sequence: pyrite \rightarrow pyrrhotite \rightarrow troilite (FeS) \rightarrow Fe, and this process is controlled by the temperature and total sulphur gas pressure in the system. Moreover, (Hong et al., 1997) believed that the thermal decomposition of pyrite is divided into two steps: (i) the first step is the decomposition of pyrite into pyrrhotite and liquid sulphur, and (ii) the second step is the formation of S_2 (g) by the combination of liquid sulphur and evaporation (Changshun et al., 2022), in agreement with (Hara, 2014).

The effect of the initial sulphur content of the cinders and treatment time on their final sulphur content after oxidation was reported by (Chun et al., 2011). Cinders were diluted with magnetite in the form of pellets to adjust the sulphur content between 0.270 and 0.455 %, and subjected to high temperature at atmospheric oxygen partial pressure. They reported that sulphur was mainly in elemental form and 95.82% of it was removed at 1503 K through simple oxidation, but this desulphurization drops with increased initial sulphur content of pellets. The desulphurization kinetics of unfluxed and fluxed pellets having sulphur range 0.16-0.75% was

reported by (Abzalov et al., 2008), in slightly oxidative and neutral environment, based on thermodynamic and reactions, their observation agreed with the unfluxed pellets by describing the sulphur removal mechanism as oxidation but in their case, they considered the oxidation of sulphide and not of elemental sulphur (Denis, 2015). In addition, above 1272 K, the higher desulphurization of the pellet was attributed to earlier decomposition between 773 and 873K according to reaction in Eq. (7), followed by interaction between the secondary sulphide and magnetite and/or heamatite in non - oxidative environment according to reactions presented in Eq. (8), (9) and (10) as well as the wustite oxidation according to Eq. (11):

$$2FeS_2 + 3Fe_3O_4 = 4Fe_2O_3 + 3FeS + \frac{1}{2}S_2 \quad \Delta G_T = -171.15 - 1.416T \text{ kJ/mol}$$
 (7)

FeS + Fe₃O₄ = 4FeO +
$$\frac{1}{2}S_2$$
 $\Delta G_T = 202.3 - 107.1$ T kJ/mol (8)

FeS + Fe₃O₄ = 4FeO +
$$\frac{2}{2}$$
S₂ $\Delta G_T = 202.3 - 107.1$ T kJ/mol (8)
FeS + 3Fe₃O₄ = 10FeO + SO₂ $\Delta G_T = 462.8 - 263.4$ T kJ/mol (9)

FeS + 4Fe₂O₃ = FeSO₄ + 8FeO
$$\Delta G_T = 378.152 - 545.006T \frac{kJ}{mol}$$
 (10)

$$4.5 \text{FeO} + 0.75 \text{SO}_2 = 1.5 \text{Fe}_3 \text{O}_4 + 0.375 \text{ S}_2 \quad \Delta G_T = -195.375 + 117.225 \text{T kJ/mol}$$
 (11)

1.2 Ion exchange

Metal sulphides interact with lime through iron exchange reactions in Eq. (12) MS(s,l) + CaO(s) = MO(s,l) + CaS(s)(12)

These reactions depend on thermal stability of metal oxide compared to its sulphide which is directly linked to the ionic radius $r_{0^{2-}} = 0.14$ nm and $r_{S^{2-}} = 0.184$ nm according to the Born - Landé Eq. (13).

$$E_{\text{lattice}} = \frac{-N_{\text{A}}MZ^{+}Z^{-}e^{2}}{4\pi\epsilon_{0}r_{0}} \left(1 - \frac{1}{n}\right)$$
 (13)

Where E_{lattice} is the lattice energy (kJ/mol, N_A the Avogadro's constant, M the Madelung constant related to crystal geometry, r_0 the interionic distance, Z^+ and Z^- the cationic and anionic charges, ε_0 is the permittivity of free space, e the electric charge 1.6022 x 10⁻¹⁹ Coulomb, and n the Born exponent. Higher Lattice energy correspond to higher mineral stability (Norman, 2021). In neutral condition lime react with pyrite according combined Eq. (14) and (15).

$$4.5 \text{FeS}_2 + 8 \text{ CaO} = 1.5 \text{Fe}_3 \text{O}_4 + 8 \text{CaS} + \text{SO}_2$$
 $\Delta G_T = -272.35 - 3.99 \text{T kJ/mol}$ (14)
 $2.625 \text{S}_2 + 3.5 \text{CaO} = 3.5 \text{ CaS} + 1.75 \text{ SO}_2$ $\Delta G_T = 477.79 - 0.63 \text{T kJ/mol}$ (15)

$$2.625S_2 + 3.5CaO = 3.5 CaS + 1.75 SO_2$$
 $\Delta G_T = 477.79 - 0.63T \text{ kJ/mol}$ (15)

Fluxed pellets contain iron sulphides and oxides associated with lime which regulates the basicity of the raw material to the iron extraction industry. The fluxed pellets desulphurization was also reported by (Abzalov et al., 2008), ion exchange reactions were identified and thermodynamic mechanisms were established. They suggested that in neutral atmosphere, above 873K, the desulphurization is slow due to the formation of calcium sulfide and iron sulphates according to reactions presented in Eq. (16) and (10):

FeS + CaO = FeO + CaS
$$\Delta G_{1273K} = 243.40 - 163.90 \text{ kJ/mol}$$
 (16)

However these sulfates begin to dissociate in temperature interval 1323K–1373K according to reaction in Eq. (17), at a rate which is sharply dependent of the temperature leading to acceleration of desulphurization.

$$2FeSO_4 = Fe_2O_3 + 2SO_2 + \frac{1}{2}O_2 \quad \Delta G_T = 912.83 - 0.62T \text{ kJ/mol}$$
 (17)

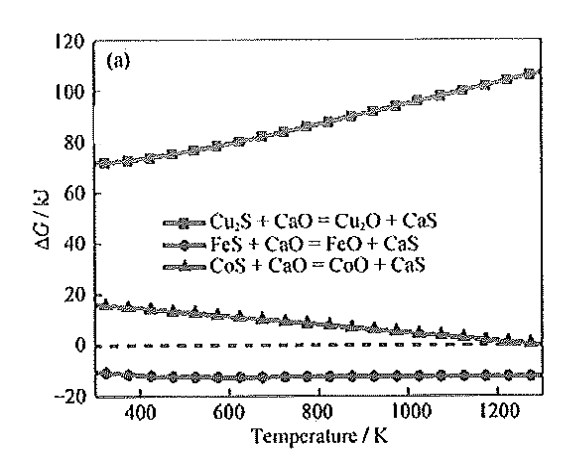


Figure 1. Free energy against temperature for the IE between sulphide and CaO (Hara 2014).

The study notes that above 1373K the temperature is the main factor reducing the sulphur content in the final fluxed pellets and residual sulphur content goes below 0.07%. The increase of heating time, is associated with the time required for assimilation of lime and the formation of slag binder above 1373K. In non-oxidative and weakly oxidative media, calcium-sulphate formation is unlikely (Abzalov et al., 2008).

In his investigations on interaction between complex sulphides and calcium oxides, (Hara, 2014) reported the free energies of the ion exchange, it is clear from Figure 1; in relation to iron, that ion exchange reaction is possible in all temperature ranges, however, introducing lime in pyrite containing material, more liquid phase at high temperature appear; this liquid phase blocks the primary iron-sulphide grains and hinders the diffusion toward the reaction surface and the diffusion of gaseous sulphur oxides from the center of reactions.

1.3 Carbothermic reduction of sulphide minerals

Mineral sulphide Carbothermic reduction is heterogeneous as presented in reactions Eq. (18), it combines solid - gas and liquid - gas reactions which occur at phase boundaries, through mass and heat transfer.

$$MS(sl) + CaO + C = M(s,l) + CaS(s) + CO(g)$$

$$(18)$$

The conditions change in the course of reaction but the rate controlling step remains the chemical reaction. The mineral sulphide configuration obeys the generalized grain model: porous solid consists of small non-porous grains of a uniform size reacting according to the shrinking - core model for iso – thermal process, meaning that reaction starts at the outer skin of the particle, the reaction zone then moves into the particle, leaving behind completely converted material and inert solid "ash." Thus, at any time there is an unreacted core of material which shrinks in size during reaction. When chemical reaction control the kinetics, the rate is proportional to the available surface of unreacted core and is given by the first-order reaction rate in Eq. (19) (Jiann, 2013; Levenspiel, 1999):

$$\frac{t}{\tau} = 1 - \frac{r_c}{R} = (1 - X_B)^{\frac{1}{3}} \tag{19}$$

Where X_B is the mole fraction of the reacted core of particle B, R: the initial radius of the core, where r_c is the radius of the core at time t, τ the time required for complete conversion.

Iron was metallised from two complex sulphides consisting of FeS₂, Cu₅FeS₄, Cu₂S, CuCo₂S₄ where copper represented 22.41 % and pyrite 15.5 %, thermal decomposition, ion exchange and Carbothermic reduction were reported. Under reducing or slightly oxidizing condition lime acts as a sulphur absorber and yields solid phases CaS or CaSO₄ and using HSC software, (Hara, 2014) suggested the trends plotted in figure 2 for the carbo-thermic reduction. This figure shows that the carbo-thermic reduction of iron sulphides is only possible above 900K. More detailed thermodynamic considerations of the same reactions mechanisms were reported. In both The main reaction for the pyrite carbothermic reduction is presented in Eq. (20). It is noted however, that at carbothermic stage, thermal decomposition and iron exchange take place as well, and thermal decomposition is the fastest and covers 20% of the treatment time, therefore the sulphur content from Eq. (3) interact as shows reaction in Eq. (21) followed by metallization in Eq. (22)

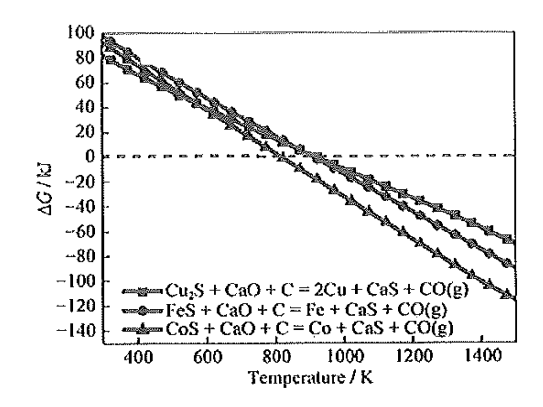


Figure 2. Free energy change against temperature for the sulphides ion exchange (Hara, 2014)

FeS + CaO + C = Fe + CaS + CO
$$\Delta G_{1273K} = 127.66 - 39.0 \text{T 1kJ/mol}$$
 (20)
2CaO + S₂ + 2C = 2CaS + 2CO(g) $\Delta G_{1273K} = 104.76 - 0.37 \text{T kJ/mol}$ (21)

Through the process in Eq. (14), (15) and (16), it was noticed that the weight loss was more than the weight of volatile substance, this was attributed to excessive amount of SO₂ gas evolved. Calcium ferrite were reported due to calcium oxide.

$$3Fe_3O_4 + 8CaO = Fe + 4Ca_2Fe_2O_3$$
 (22)

$$5Fe + 8CaSO_4 + Fe_3O_4 = 4Ca_2Fe_2O_5 + 8SO_2$$
 (23)

Nonferrous minerals such chalcocite (Cu₂S) play synergetic and catalytic role of ferrite reaction in Eq. (24), and favoring the formation through Eq. (25) of intermediate phase Ca₂CuFeO₃S, which speeded up the metallization process according to reactions in Eq. (26):

$$Cu_2S + CaO = Cu_2O + CaS (24)$$

$$Cu2O + CaS + Ca2Fe2O5 = 2Ca2CuFeO3S$$
 (25)

$$Ca_2CuFeO_3S + 2C = Cu + Fe + CaS + CaO + 2CO$$
 (26)

In addition, due to prevailing thermodynamic conditions (Branan, 2023; Yaws, 2023;), Eq. (22) and (23) are favoured by the presence of iron oxides between 773 and 973K, as

intermediate phases, they are directly or indirectly reduced to metal according to reaction in Eq. (2) and (27 - 30) (Hara, 2013).

$$Fe_3O_4 + 4CO = 3Fe + 4CO_2$$
 $\Delta G_T = -8.03 - 0.02T \text{ kJ. mol}^{-1}$ (27)

$$\begin{aligned} \text{Fe}_3 \text{O}_4 + 4\text{CO} &= 3\text{Fe} + 4\text{CO}_2 \\ 3\text{Fe}_2 \text{O}_3 + \text{CO} &= 2\text{Fe}_3 \text{O}_4 + \text{CO}_2 \\ \text{Fe}_3 \text{O}_4 + \text{CO} &= 3\text{FeO} + \text{CO}_2 \end{aligned} \qquad \begin{aligned} \Delta G_T &= -8.03 - 0.02\text{T kJ. mol}^{-1} \\ \Delta G_T &= -43.00 - 52\text{T kJ. mol}^{-1} \end{aligned} \qquad (28) \\ \Delta G_T &= 30.2 - 29.2\text{T kJ. mol}^{-1} \end{aligned} \qquad (29) \\ \Delta G_T &= -22.8 - 24.26\text{T J. mol}^{-1} \end{aligned} \qquad (30)$$

$$Fe_3O_4 + CO = 3FeO + CO_2 (g)$$
 $\Delta G_T = 30.2 - 29.2 \text{T kJ. mol}^{-1}$ (29)

$$FeO + CO = Fe + CO_2$$
 $\Delta G_T = -22.8 - 24.26 \text{T J. mol}^{-1}$ (30)

The carbon dioxide from reaction in Eq. (2), (27) and (30) reacts with carbon through Boudouard reaction in Eq. (31) to form carbon monoxide which increases its concentration and improves indirect reduction (Vandana et al., 2014).

$$C(s) + CO_2(g) = 2CO(g)$$
 $\Delta G_T = 166.52 - 171.1 \text{ T}$ (31)

Since ion - exchange reactions in Eq. (14) and (16) are faster than metal oxide reduction in Eq. (30); metal oxide layer surounds sulphide grains and makes the last step of carbothermic reduction a simple direct and indirect reduction of metal oxide. Carbothermic reduction of sulphide was established at an optimum ratio metal sulphide, lime and carbon ratio (MS: CaO: C=1:2:2) with iron metallization directly from pyrite concentrate involving possibility of capturing the sulphur into a solid phase, this approach is economical and environmentally friendly though methods are yet to be thoroughly established for industrial application. In both (Hara, 2013) and (Hara, 2014), studies were conducted on complex sulphide which systematically differs from the application in this study where pyrite concentrate is used and nonferrous metals are in very negligible concentrations. Therefore, this paper investigates the iron metallization from an isolated high grade pyrite concentrate in which nonferrous minerals are in negligible amounts using the analytical aspect of the process. The prospection of sulphide ores, containing magnetite and pyrrhotite is done by mean of magnetic methods because they have a large magnetic expression. Worm (1999) and his colleagues state that the susceptibility of pyrrhotite and its field dependence increase strongly with grain size (Worm et al., 1999).

2 MATERIALS AND METHODS

2.1 Sample Collection and Preparation

Pyrite concentrate samples were collected from stockpiles at the Otjihase Concentration Plant, where several years of production had been accumulated. To ensure a systematic and representative sampling process, a simplification of boundary condition technique approach was employed. The stockpiles were approximated as trapezoidal heaps measuring 15 m in length, 5 m in height, and 7 m in width, yielding a total trapezoidal surface area of 188 m².

Each heap was partitioned into a 1 m × 1 m grid pattern, and a 0.9 m-long, 40 mm-diameter sampling spear was inserted to a depth of 0.5 m at each grid point to extract 188 increments of 0.35 kg each. Sampling was performed across four heaps to enhance representativeness. The collected increments were homogenized, dried, and mechanically rolled before screening to a particle size of ≤150 µm using a standard sieving method. The Laser Particle Size Analyser (BT-9300H) determined the p84 value of 37.75 μm, confirming a fine particle size suitable for reaction kinetics analysis.

2.2 Blending and Sample Classification

The screened pyrite concentrate was blended with 98% purity CaO lime (powder) and 56% carbon coal (150 µm) in varying ratios to form seven distinct categories of 150 g each. The blended compositions are summarized in Table 1. The chemical composition of each category was analyzed using:

Table 1. Compositions of blended pyrite, lime and coal corresponding to 150 g of each

_	Category	Mg	Si	S	Ca	Mn	Fe	Co	Ni	Cu	Zn
-	1	7.042	1.807	48.04	0.756		42.097	0.084	0.020	0.125	0.024
	2	5.139	1.442	33.613	14.601		34.909	0.066	0.017	0.093	0.019
	3	2.143	2.082	35.398	17.214	0.057	36.711	0.103	0.019	0.055	0.029
	4	1.072	1.964	37.094	15.664	0.028	39.656	0.051	0.032	0.080	0.031
	5	3.578	1.901	37.915	10.688	0.054	41.132		0.032	0.115	0.034
	6	5.213	1.571	31.291	17.640	0.039	33.883	0.024	0.024	0.081	0.026
	7	6.627	1.468	33.241	18.969	0.044	32.330	0.075	0.010	0.081	0.017

- Atomic Absorption Spectrometer (AAS) (Mark NOVA, S 113A0386) for elemental analysis,
- X-ray Fluorescence (XRF) Spectrometer (TITAN BRUKER) for oxide composition, and
- Sulphur and Carbon Analyzer (LECO S-144DR) for sulphur and carbon quantification.

Each 150 g category was further subdivided using a 6 mm spacing riffle splitter, yielding 25 sub-samples of 6 g each. An electronic balance (RADWAG WAI ELEKTRONICZNE, Model AS 60/220/C/2) ensured precise weighing. Figure 3 presents the flow chart of the sample preparation process.

The mineralogical composition of each category was determined based on mass balance considerations, accounting for the thermal stability of FeO at high temperatures (Table 2), while the molar ratios of FeS₂, CaO, and carbon (C) were computed and summarized in Table 3.

Table 2. Mineral composition of the original blended samples

Series No	FeS ₂ (%)	Fe ₂ O ₃ (%)	$CuFeS_{2}(\%)$	ZnS (%)	Theoretical lost
1	89.818	0.103	0.361	0.035	23.977
2	62.832	7.865	0.268	0.028	16.774
3	66.242	8.215	0.158	0.043	17.675
4	69.373	10.303	0.231	0.046	18.515
5	70.844	11.387	0.330	0.051	18.915
6	58.495	9.307	0.233	0.039	15.615
7	62.159	4.645	0.233	0.025	16.592

Table 3. Mineral composition of the original blended samples (Continued)

Series No	CaO (%)	C (%)	FeS ₂ – CaO – C-
1	0.000	0.00	1-0-0
2	29.37	0.00	1:1.4:0
3	12.86	7.35	1:0.6:1.5
4	8.79	7.70	1:0.4:1.4
5	6.81	7.87	1:0.3:1.4
6	22.74	6.50	1:1.3:1.7
7	18.05	6.90	1:0.9:1.6

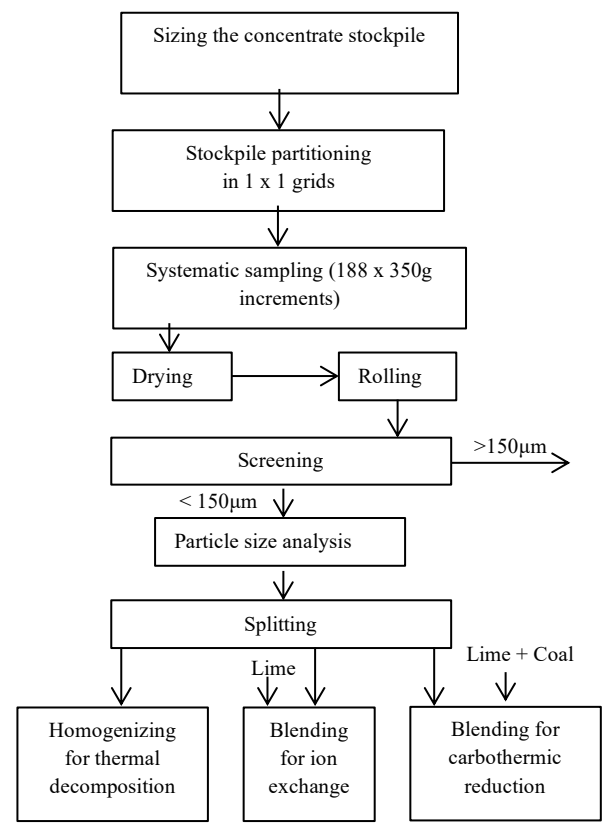


Figure 3. Sample preparation flow chart

2.3 Experimental Design and Procedure

Three distinct experimental stages were considered:

- Stage 1: Thermal decomposition of pyrite,
- Stage 2: Ion exchange reactions between FeS₂ and CaO,
- Stage 3: Carbothermic reduction in the presence of carbon and lime.

Samples were treated in a Nabertherm N300 muffle furnace under reducing conditions. Once the samples were loaded, the furnace door was sealed, and the air circulation was cut off by closing the airflow gate. The samples were heated to 1273K, 1373K, and 1473K at a controlled rate of 5 K/min.

- Thermal decomposition and ion exchange experiments involved 15 samples per stage, corresponding to two factors:
 - o **Time** (5, 10, 15, 20, and 25 min)
 - o **Temperature** (1273K, 1373K, and 1473K).
- Carbothermic reduction experiments involved 75 samples, corresponding to three factors:
 - o Carbon-to-lime ratio (C/CaO) (five levels),
 - o Time (5, 10, 15, 20, and 25 min),
 - Temperature (1273K, 1373K, and 1473K).

Each 6 g sample was placed in a 5.9 cm³ zirconium crucible, covered to minimize oxidation, and held at the target temperature for the designated treatment time. Post-reaction, the crucibles were rapidly cooled, and the residues were weighed to assess mass loss. The treated samples were sealed in airtight plastic bags and stored in a desiccator to prevent moisture absorption.

2.4 Data Analysis

The mass percent reduction (R%) was calculated to quantify iron metallization. The chemical and mineralogical changes were analyzed using:

- XRF for elemental composition,
- AAS for iron quantification,
- LECO S-144DR for sulphur retention,
- Magnetic susceptibility tests to assess phase transformations.

Statistical analyses included:

- Analysis of Variance (ANOVA) at a 95% confidence level to assess the significance of experimental variables,
- **Pearson correlation tests** to evaluate the relationships between temperature, treatment time, and mass reduction,
- Regression modeling for trend simulation,
- Integral method of metallurgical kinetics to determine reaction orders.

3. RESULTS

This section presents the findings from the three experimental stages: thermal decomposition, ion exchange, and carbothermic reduction, where iron and sulphur content were analyzed. ANOVA statistical analysis was performed using Microsoft Excel at a 95% confidence level, with a significance threshold of $\alpha=0.05$, to determine the statistical relevance of the experimental factors. Additionally, regression modeling was employed to simulate trends using a logarithmic scale.

3.1 Thermal Decomposition

The iron and sulphur content of the samples subjected to thermal decomposition were determined via X-ray Fluorescence (XRF) and plotted against treatment time at 1273K, 1373K, and 1473K (Figure 4). The ANOVA test yielded a p-value of 0.013, which is significantly lower than 0.05, indicating that treatment time had a systematic and statistically significant effect on the iron and sulphur content of the pyrite concentrate.

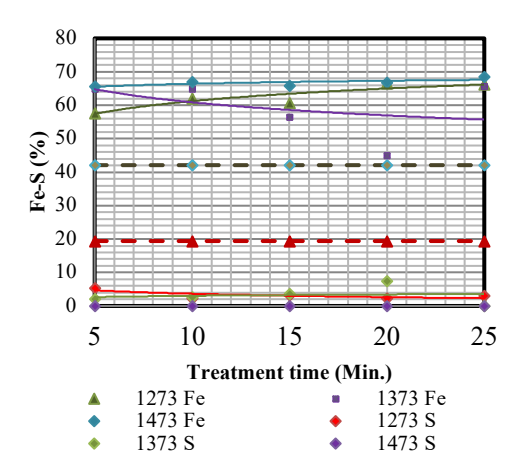


Figure 4. Iron & Sulphur (%) against
Time at different temperatures
for the thermal decomposition

At 1273K and 1473K, the iron content increased with treatment time, whereas at 1373K, an initial increase was followed by stabilization, suggesting a reaction limitation due to liquid phase formation. The sulphur content showed a consistent decrease across all temperatures, confirming the progressive volatilization of sulphur during decomposition.

3.2 Ion Exchange Reactions

The iron and sulphur content of samples treated under ion exchange conditions were analyzed via XRF and plotted against treatment time at 1273K, 1373K, and 1473K (Figure 5). The ANOVA test yielded a p-value of 0.005, confirming a statistically significant effect of treatment time on the iron and sulphur content.

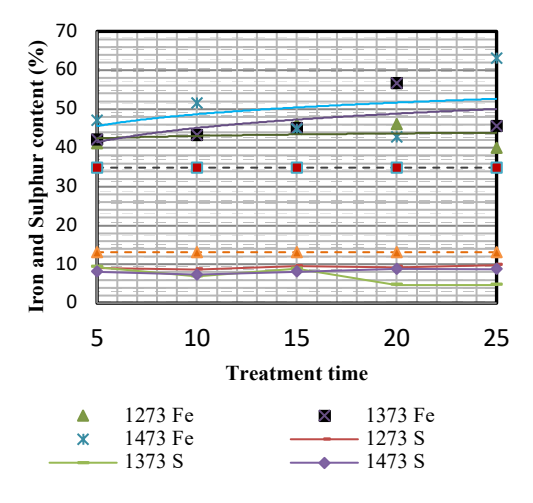


Figure 5. Iron and sulphur content against time for iron exchange (29.47% lime) at different temperatures at ion exchange

Iron content increased at all temperatures, but the rate of increase was lower than in the thermal decomposition stage, indicating sulphur capture within the solid residue rather than complete

volatilization. The sulphur content showed a decreasing trend, with higher CaS formation observed at 1473K, confirming the effectiveness of lime in capturing sulphur.

3.3 Magnetic Behavior of the Samples

All treated samples were subjected to a magnetic field, and their response was recorded. The original pyrite concentrate exhibited no magnetic behavior, confirming the absence of magnetic phases in its untreated form. However, certain treated samples displayed strong magnetic susceptibility, with their iron content summarized in Table 4.

Table 4. Iron content of samples that displayed magnetic susceptibility

		Lime (%)		
1273K	0	8.8	11.6	17.8
5 Minutes	-	-	49.96	50.02
10 Minutes	62.11	-	55.33	55.13
15 Minutes	60.79	-	54.5	48.45
20 Minutes	66.7	-	58.16	57.86
25 Minutes	66.21	53.32	55.95	55.77
1373K	-	-	-	-
5 Minutes	64.84	-	-	-

A representative sample containing 17.8% CaO, treated at 1373K, was visually examined, revealing the distinctive red coloration of hematite (Fe₂O₃) (Figure 6). The magnetic response was further analyzed by plotting the number of samples exhibiting magnetic behavior against temperature (Figure 7). Samples treated at lower temperatures exhibited higher magnetic susceptibility, which decreased at 1473K, likely due to the transformation of iron-bearing phases into non-magnetic compounds.



Figure 6. Characteristic image of the heamatite for the the samples consisting 17.8% lime and treated at 1373K

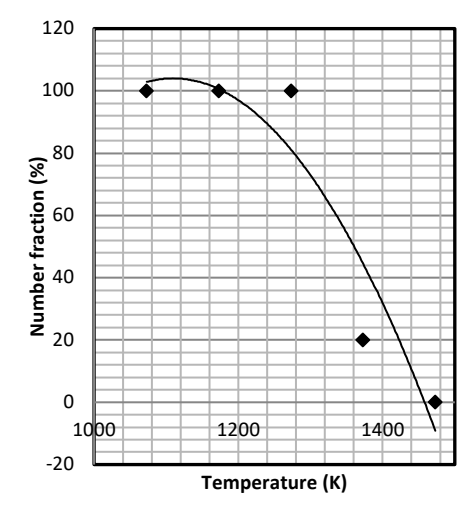
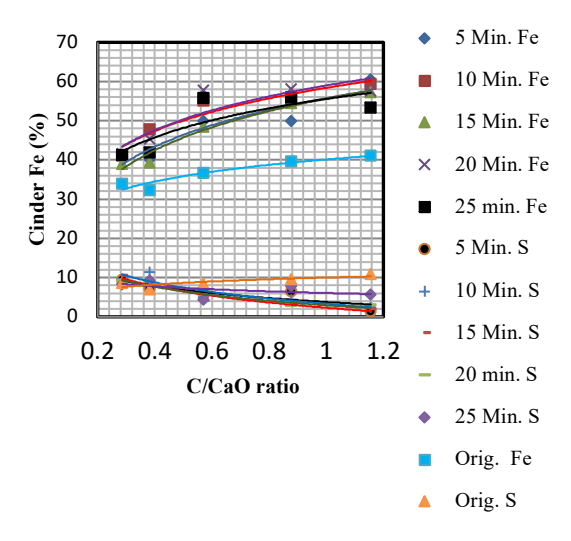


Figure 7. Number fraction of samples that exhibited magnetic behaviour against temperature

3.4 Carbothermic Reduction

The iron and sulphur content of the carbothermically reduced samples were analyzed and plotted against the C/CaO ratio at different treatment times. The results are presented in Figures 8, 9, and 10, corresponding to reduction at 1273K, 1373K, and 1473K, respectively.



70 5 Min. Fe 60 10 Min. Fe **3**50 15 Min. Fe 20 Min. Fe 26 Min. Fe 5 Min. S 10 10 Min. S 0 15 Min. S 0.2 0.4 0.6 0.8 1 C/CaO moles ratio

Figure 8. Iron and sulphur (%)
against C/CaO
ratio (w/w) at 1273K
and different
treatment
times

Figure 9. Iron and sulphur (%) against C/CaO ratio (w/w) at 1373K and different treatment Times

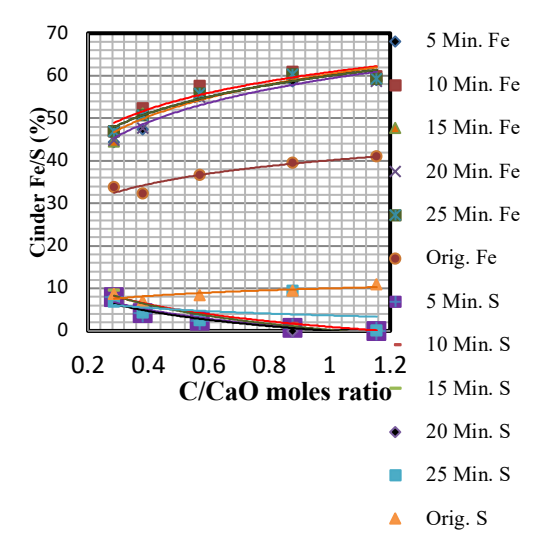


Figure 10. Iron and sulphur (%) against C/CaO ratio (w/w) at 1473K and different treatment Times

At 1273K, iron content increased with an increase in C/CaO ratio up to a certain limit, after which the trend plateaued, suggesting a reaction-limiting factor such as poor gas diffusion. Sulphur content decreased steadily, indicating the effectiveness of carbon reduction at lower temperatures.

At 1373K, the iron content showed an increasing trend but at a reduced rate compared to 1273K, likely due to partial liquid phase formation, which hindered gas—solid interactions. The sulphur content decreased more gradually, suggesting retention of sulphur in the solid phase as CaS.

At 1473K, iron content reached its highest levels, confirming enhanced metallization at higher temperatures. However, the liquid phase formation significantly slowed reaction kinetics, leading to reduced diffusion-driven reduction mechanisms. The sulphur content exhibited a sharp decline, indicating near-complete removal, either as gaseous SO₂ or as retained CaS in the residue.

4. DISCUSSION

The results from the thermal decomposition, ion exchange, and carbothermic reduction stages were interpreted, focusing on their impact on iron concentration, sulphur retention, and reaction kinetics. Additionally, the magnetic susceptibility of treated samples is analyzed to determine phase transformations in the pyrite concentrate.

4.1 Thermal Decomposition Stage

As illustrated in Figure 4, the iron concentration in the cinder increased with treatment time at 1273 K and 1473 K. However, at 1373 K, the trend was reversed, suggesting a disruption in reaction kinetics—possibly due to the formation of a liquid phase. Higher temperature treatments yielded higher iron grades, as evidenced by the high-temperature curves lying above those of lower temperatures. This observation aligns with the findings of Changshun (2022). The maximum iron concentration of 68.59% was obtained at 1473K after 25 minutes, indicating that thermal decomposition significantly enhanced iron content in the cinder.

All sulphur concentration curves declined with increasing treatment time, confirming that sulphur was progressively eliminated from the cinder. Additionally, the sulphur content at all temperatures was lower than that of the original pyrite concentrate, affirming that thermal decomposition effectively removed sulphur. Figure 4 further illustrates that higher temperatures resulted in lower sulphur retention, aligning with the findings of Abzalov (2008).

At 1473K, sulphur was completely depleted within 5 minutes, suggesting that high-purity iron can be recovered from pyrite under these conditions. The metallurgical kinetics analysis revealed that thermal decomposition follows zero-order kinetics with respect to iron at 1273K, while at 1373K and 1473K, the process follows second-order kinetics. These results partially agree with Changshun et al. (2022), who reported a first-order kinetic model for thermal decomposition.

4.2 Magnetic Behaviour

No samples treated at 1473K exhibited magnetic susceptibility, despite their higher iron content, while cinders from samples treated below 1373K showed magnetic properties. This

behavior can be attributed to the presence of pyrrhotite (Fe_{1-x}S) at lower temperatures, which is transformed into wüstite (FeO) and lower iron sulphates at higher temperatures, as suggested by Abzalov (2008) and Worm (1993).

At the carbothermic stage, only samples with a C/CaO ratio of 0.571 or higher exhibited magnetic properties at 1273K. However, the number of magnetic samples decreased as the ratio increased, and at 1.156, only one sample remained magnetic. At higher temperatures, no samples exhibited magnetic behavior, suggesting that pyrrhotite concentration decreased, and iron metallization remained insufficient due to longer diffusion distances required for reduction reactions.

4.3 Ion Exchange Reactions

Approximately 80% of the treated samples showed an increase in iron concentration, but the rate of increase was relatively low, as depicted in Figure 5. The prolonged exposure to ion exchange reactions contributed to gradual iron enrichment, consistent with the loss of sulphur in the form of SO₂ gas, as described by Equation (14). The stability of sulphides compared to oxides aligns with the findings of Norman (2021).

The iron concentration curves remained above the original concentration, indicating that ion exchange facilitated iron enrichment. The higher temperature treatments resulted in higher residual iron concentration, supporting the conclusions of Vandana (2015).

However, the sulphur content trends exhibited a slightly decreasing behavior, except at 1273K and 1473K, where the curves flattened (Figure 5). The sulphur content of all treated samples remained lower than the original pyrite concentrate, confirming that sulphur was effectively removed in the form of SO₂or S₂, consistent with Absalov (2008). The residual sulphur content was higher in ion exchange reactions than in thermal decomposition, likely due to sulphur retention as CaS, as suggested by Changshun (2022) and confirmed by Equations (16), (14), and (15).

4.4 Carbothermic Reduction Stage

At all temperatures, iron concentration increased with an increasing C/CaO ratio, while sulphur content declined. However, the curves flattened above a C/CaO ratio of 0.7, as shown in Figures 8, 9, and 10.

Beyond thermal decomposition and ion exchange, the increased C/CaO ratio contributed to iron metallization by enhancing carbon distribution and improving CO circulation. However, the flattening of the curves could be attributed to three factors:

- 1. Reduced diffusion kinetics of carbon and CO through the oxide layer toward the reaction center.
- 2. Limited migration of lime molecules toward the sulphide core.
- 3. Thermodynamic constraints on reaction interfaces, as suggested by Levenspiel (1999) and Jiann (2013).

As temperature increased, the growth rate of iron concentration slowed, possibly due to liquid phase nucleation facilitated by lime, which restricted atomic mobility. All treated samples had a higher iron concentration than the original pyrite concentrate, confirming the effectiveness of

carbothermic reduction. This observation is consistent with previous findings by Levenspiel (1999), Jiann (2013), Hara (2013, 2014), who characterized carbothermic reduction kinetics using the shrinking-core model, described by Equation (19).

In general, samples treated for shorter durations exhibited lower iron concentrations, while longer treatment times resulted in increased iron content, aligning with Abzalov (2008), who attributed this trend to the time required for lime assimilation and slag formation above 1373K.

The partial reduction in sulphur content may be explained by:

- S₂ evolution during thermal decomposition and ion exchange reactions, as described by Equations (5), (6) and (14)
- Sulphur retention in the solid residue as CaS, as shown in Equations (20) and (21).

5 CONCLUSIONS

This study explored the carbothermic reduction of pyrite in the presence of lime, focusing on iron metallization, sulphur retention, reaction kinetics, and magnetic behavior. The findings demonstrated that thermal decomposition led to a maximum iron concentration of 68.59% at 1473K, with complete sulphur depletion within 5 minutes, following zero-order kinetics at 1273K and second-order kinetics at higher temperatures. Ion exchange reactions facilitated sulphur capture as CaS, reducing SO₂ emissions, while carbothermic reduction enhanced iron metallization, though liquid phase formation at higher temperatures restricted reaction kinetics. The magnetic susceptibility decreased with temperature, confirming pyrrhotite transformation into non-magnetic phases. These results suggest a sustainable pathway for utilizing pyrite waste as a secondary iron source, reducing reliance on high-grade iron ores while minimizing sulphur emissions. This process aligns with cleaner metallurgical practices, promoting waste-to-resource conversion and enabling circular economy applications through by-product utilization in cement and gypsum industries. Future work should focus on industrial-scale optimization, refining the C/CaO ratio, and exploring alternative reducing agents to further enhance process efficiency and sustainability in iron production.

ACKNOWLEDGEMENTS

The authors acknowledge the Mechanical and Metallurgical Engineering of the University of Namibia for hosting the research and the Royal Academy of Engineering for fundinding this project, Dr. Johannes Petrinna, Associate dean of the Faculty of Engineering and the built Environment for for owning the admistrative aspect of the project, Mr. Raymond Hulbert, Mr. Andrew Thomson and Mr. Craig Thomas respectively Central Operations manager, Executive Technical Director and Chief Executive Officer of Weatherly Mining Namibia for backing this project and providing samples and other relevant materials for the research.

REFERENCES

- [1] Abdrakhimov A.V., Abdrakhimova E.S., Abdrakhimov V.Z., 2006. Technical properties of roof tiles made of technogenic material with pyrite cinder, *Glass and Ceramics*, 63, 3 4.
- [2] Abzalov V. M., Sundai A. V., Yur'ev B. P., 2008. Desulphurization in roasting iron Ore pellets, *Steel in Translation 38*, 1003-1007.
- [3] Ahindra G., Amit C., 2008. Ironmaking and steel making, theory and practice, PHI Learning, New Delhi.

- [4] Alpi I., Deveci H., Yazici E. Y., Türk T., Y. H. Süngün Y. H., 2009. Potential use of pyrite cinders as raw material in cement production: results of industrial scale trial operations. *Journal of hazardous materials* 166, 144-149.
- [5] Bai G., Zhou X., 2009. Study on Pelletizing of pyrite cinder with magnetite, *Iron Steel*, 1, 4-0.
- [6] Branan C. R., Rules of Thumb for Chemical Engineers, A Manual of Quick, Accurate Solutions to Everyday Process Engineering Problems (4th Edition), https://app.knovel.com, accessed: November , 2023.
- [7] Changshun T., Unzhang R., Gang S., Huang T., Xiang C., 2022. The Thermal Decomposition Behavior of Pyrite-Pyrrhotite Mixtures in Nitrogen Atmosphere, *Journal of Chemistry*, 2022, 11.
- [8] Chun T., Zhu D., Pan J., 2011. Influence of sulfur content in raw materials on oxidized pellets, *Journal of Central South University of Technology 18*, 1924-1929.
- [9] Denis S. Evgueni J, Sergei A., 2015. Critical Assessment and Thermodynamic Modeling of the Fe-O-S System, *Journal of Phase Equilibrium and Diffusion 36*, 224-240.
- [10] Dorin B., Nigel J. B., 2015. Acid mine drainage: electrochemical approaches to prevention and remediation of acidity and toxic metal, *Journal of Applied Electrochemistry*, 45, 1239-1254.
- [11] Giunti M., Baroni D., Bacci E., 2004. Hazard assessment to workers of trace metal content in pyrite cinders, *Bulletin of Environmental Contamination and Toxicology*, 72, 352–357.
- [12] Hara S. R. H., 2013. Study of Reaction Mechanisms for Copper-Cobalt-Iron Sulfide Concentrates in the Presence of Lime and Carbon, *Journal of the Minerals, Metals & Materials Society* 65, 1597-1607.
- [13] Hara S. R. H., 2014. Mineral sulphide-lime reactions and effect of CaO/C mole ratio during carbothermic reduction of complex mineral sulphides, *International Journal of Minerals, Metallurgy and Materials 21*, 1.
- [12] Hong, Y. and Fegley Jr, B., 1997. The kinetics and mechanism of pyrite thermal decomposition. *Berichte der Bunsengesellschaft für physikalische Chemie*, 101(12), pp.1870-1881.
- [13] Hongming L. T., Chun T., Zhanxia D., Wang P., Meng Q., Jiaxin L., 2004. Preparation of metallic iron powder from pyrite cinder by Carbothermic reduction and magnetic separation, *Metals*, 6, 88.
- [14] James R. M., Julie B. Z., 2010. Environmental Engineering, fundamentals, sustainability, design, USA.
- [15] Jiann Y. B., 2013. Characterization of Minerals, Metals, and Materials, Presented at Symposium, Held during the TMS Annual Meeting and Exhibition, San Antonio, Texas, USA, March 3-7.
- [16] Kama M., Kama N., Leki P., 2021. Production of Sponge Iron from the Ok Tedi Pyrite concentrates, *International Journal of Science and Academic Research* 2, 1451-1455.
- [17] Kipp D. O., (2018). MatWeb Ceramics Material Data Sheets (MDS). MatWeb, LLC, https://app.knovel.com, accessed: November, 2023.
- [18] Knovel, Properties of elements, Plastics Design, https://app-knovel-com, accessed: November, 2023.
- [19] Knovel, Physical Constants of Inorganic Compounds, https://app-knovel-com, accessed: November, 2023.
- [20] Lambert J. M., Simkovich G., Walker J. R., 1998. The kinetics and Mechanism of the pyrite to pyrrhotite Transformation, *Metallurgical and Materials Transactions B*, 29B,

385.

- [21] Levenspiel O., 1999. Chemical Reaction Engineering (3rd Edition), John Wiley & Sons, New York.
- [22] Liu Z. C., Zheng Y., 2011. Hexagonal hematite platelets synthesized from pyrite cinders by hydrothermal process. Journal of Central South University of Technology 18, 1377-1382.
- [23] Mular A. L., Halbe D. N., Barratt D. J., 2002. Presented at Mineral Processing Plant Design, Practice, and Control Proceedings, Volumes 1-2. Society for Mining, Metallurgy.
- [24] Norman N. C., 2021. Periodicity and the s- and p- Block Elements (2nd Edition), Oxford University Press. UK.
- [25] Pelovski Y., Petkova V., 1999. Investigation on thermal decomposition of pyrite part 1, *Journal of Thermal analysis and calorimetry*, 56, 95-99.
- [26] Qiang Z., Jilai X., Wen C., 2019. A novel self-Magnetizing roasting process for recovering Fe from low grade pyrite cinder and blast furnace sludge, *Transactions of the Indian Institute of Metals*, Technical paper, doi:10.1007/s12666-019-01724-x.
- [27] Rath S. S., Rao D. S. Rao., 2017. Dolochar as a reductant in the reduction roasting of iron ore slimes, *International Journal of Minerals, Metallurgy and Materials* 24, 1341.
- [28] Sun K. Lu W. K., 2009. Mathematical modelling of the kinetics of carbo-thermic reduction of iron oxides in ore-coal composite pellets. *Metallurgical and Materials Transactions B*: Process Metallurgy and Materials Processing Science 40, 91-103.
- [29] Tugrul N., Derun E.M., Pis kin M., Piskin S., 2003. Evaluation of pyrite ash wastes obtained by the sulfuric acid production industry, presented at 8th International Conference on environmental science and technology, Lemonos Island, Greece, 8-10 September, p.36.
- [30] Tugrul N., Derun E. M., Mehmet P., 2006. Effects of calcium hydroxide and calcium chloride addition to bentonite in iron ore palletisation, *Waste Management & Research*, 24, 446-455.
- [31] Tugrul N., Derun E.M., Piskin M., 2007. Utilization of pyrite ash wastes by pelletization process, *Powder Technology*, 176, 72-76.
- [32] Turkdogan E. T., 1996. Fundamentals of Steelmaking. Maney Publishing for IOM3, London, UK.
- [33] Tveit M. T., 2003. A simulation model of a sulphuric acid production process as an integrated part of an energy system, *Simulation Modellelling and Practical Theory*, 11, 585–596.
- [34] Vandana K., Gour G. R., Prodip S., 2015. Mathematical Model to Estimate the Rate Parameters and Thermal Efficiency for the Reduction of Iron Ore–Coal Composite Pellets in Multi-layer Bed at Rotary Hearth Furnace. *Transition of the Indian Institute of Metals* 68, 109-116.
- [35] Worm H. U., Clark D., Dekkers M. J., 1993. Magnetic susceptibility of pyrrhotite: grain size, field and frequency dependence, *Geophysical Journal International*, 114, 127-137.
- [36] Yaws C. L., Yaws' Handbook of Thermodynamic Properties for Hydrocarbons and Chemicals, https://app.knovel.com, accessed: November, 2023.
- [37] Zheng Y. J., Liu Z.C., 2011. Micaceous iron oxide prepared from pyrite cinders by hydrothermal method, *Journal of Central South University of Technology*, 18, 89-95.
- [38] Zheng J. L., Xiang X., Zjang J., 2012. Reduction mechanisms of pyrite cinder-carbon composite pellets, *International Journal of Minerals, Metallurgy and Materials* 19, 986-991.
- [39] Zhu D., Jian L., Jian P., Xiao X., Yong Z., Tang Y., Yu C., 2006. Study on pelletising

Hunga et al. 151314 2023 10.100-124

- of magnetite concentrate from pyrite cinder, *Journal of Mining and Metallurgical Engineering*, 26, 49 52.
- [40] Zhu D., Li J., Pan J., 2007. Preparation of high quality magnetite concentrate from pyrite cinder by composite pellet reduction-roasting and magnetic-separation, *Chinese Journal of Nonferrous Metals*, 17, 649–656.
- [41] Zorya V. N., Korovushkin V. V., Permyakov A. A., Volynkina E. P., 2015. Mineral Composition and Crystalline Structure of Iron Bearing Components in Metallurgical Waste. *Steel Translation* 45, 331-337.